



In Vitro Microstructure, Shape Memory, Corrosion, and Biocompatibility Characteristics of Porous Ti-51 at.%Ni- x Sn Shape Memory Alloys

Mustafa K. Ibrahim¹ · Safaa N. Saud² · E. Hamzah³ · E. M. Nazim³

Received: 19 June 2021 / Revised: 28 January 2022 / Accepted: 3 February 2022 / Published online: 9 March 2022
© ASM International 2022

Abstract

To examine the impact of tin (Sn) element on the microstructure and properties of biomedical β -type Ti-Ni shape memory-based alloys, porous Ti-51 at.%Ni- x Sn ($x = 0, 0.225, 0.453, \text{ and } 1.375$) alloys were investigated. The microstructure of the Sn-modified and unmodified alloys showed two main regions, viz. Ti- and Ni-rich regions, corresponding to Ti_2Ni and TiNi_3 phases, plus some intermetallic compounds (Ti_3Sn and Sn_5Ti_6) as Sn was added. The transformation temperature curves of the Ti-Ni and Ti-Ni- x Sn samples displayed a multistep phase transformation ($\beta 1' \rightarrow \text{R} \rightarrow \beta 2$) during the heating process. Addition of 0.225 at.% Sn to the Ti-51 at.%Ni sample improved its fracture strength, strain and shape memory behavior, polarization resistance, and antibacterial properties. On the other hand, the antibacterial properties further increased when the Sn content was increased to 0.453 and 1.375 at.%, although the mechanical and shape memory properties were degraded.

Keywords Ti-51 at.%Ni- x Sn SMAs · Shape memory effect · Biocompatibility · Porous · Microwave sintering

Introduction

Shape memory alloys (SMAs) offer remarkable combinations of various key features, including pseudoelasticity (PE), the shape memory effect (SME), and high damping capacity [1, 2]. Because of its unique mechanical characteristics and biocompatibility, titanium alloy is frequently used in bone substitutes. However, the overall structural stresses experienced by such artificial materials are lower than those of natural bone with an elastic modulus of 2.3–20 GPa, pore size of 20–1000 μm , and porosity of 30–95% [3]. This effect may result in bone loss and implant loosening. Mechanical effects must thus be considered; for example, when the elastic modulus of subchondral bone is substantially lower,

this problem is enhanced [4]. To address this issue, bone-like structures can be designed to allow for elasticity based on a bone-like geometric structure.

Different pore diameters may impact the biological performance of an implant, further complicating matters. Micro- and macropores play a crucial role in bone development, cell adhesion, and fluid transfer [5]. Much interest has been focused on different applications of Ti-Ni alloys on the basis of their potential utility in functional materials such as smart structures or adaptive and similar applications in biomedicine [6–8]. Ti-Ni alloys exhibit many unique features, ranging from their biological performance to their physical and chemical properties, making them suitable for use in a broad range of biomedical situations [9, 10] as a result of their exceptional superelasticity [11] and unique shape memory effect [12], as well as low elastic modulus [13]. Other characteristics that make them unique are their excellent corrosion resistance and biocompatibility [14–17], together with non-ferromagnetic nature [18]. The integration of different ternary elements into titanium alloys has demonstrated that Sn stabilizes the SME. Formation of the ω -phase and the stabilization associated with the parent β -phase are restricted by Sn [19–21]. The Ti alloy corrosion behavior is enhanced by including Sn [22].

✉ Safaa N. Saud
safaaengineer@gmail.com

¹ Faculty of Computer Engineering, University of Imam Jafar Sadeq Maysan Branch, Maysan 62012, Iraq

² Faculty of Information Sciences and Engineering, Management and Science University, Shah Alam, Selangor, Malaysia

³ Faculty of Mechanical Engineering, Universiti Teknologi Malaysia, 81310 UTM Johor Bahru, Johor, Malaysia

Nonetheless, the pore size, shape, and distribution can affect the enhancement of the mechanical properties through the shape memory effect or improved ductility, in addition to the grain size and structure, together with precipitate formation, phase morphology, and degree of order. The principal aim of this study is to explain the effect of Sn element on the microstructural characteristics and mechanical properties, as well as corrosion and antibacterial behaviors, of Ti-Ni SMAs. The results obtained will be beneficial for the development of Ti-Ni SMAs as well as their use in biomedical applications.

Experimental Procedures

Sample Preparation

We used Ti (99.5% purity), Ni (99.5%), and Sn (99.5%) elemental powders with particle size of 150, 45, and 45 μm , respectively. Ti-51Ni- x Sn powders ($x = 0.225, 0.453,$ and 1.375 at.%) were manufactured by mechanical alloying (powder metallurgy) in a planetary ball mill (PM100). The milling procedure was carried out at 300 rpm for 1 h using a powder ratio of 4:1. The mixed powders (Sn-modified and unmodified) were compressed at uniaxial pressure of 230 kg/cm^2 for 5 min to produce green samples. Thereafter, a microwave sintering system (MWS, HAMiLab-V3, SYNOTHERM Corp.) was utilized for sintering, which included heating the green samples for 15 min at $700 \text{ }^\circ\text{C}$ with a heating rate of 30°C/min . The sintered samples were then cut using an electrical discharge machining (EDM) wire cutter to $7 \times 7 \times 14 \text{ mm}^3$ for compression testing according to ASTM E9-09, $10 \times 10 \times 20 \text{ mm}^3$ for shape memory testing, and $\Phi 13.5 \times 2 \text{ mm}$ and $\Phi 5 \times 1.5 \text{ mm}$ for corrosion and antibacterial tests, respectively.

Microstructural Characterization

The sintered samples were characterized by scanning electron microscopy (Hitachi S-3400N) equipped with energy dispersive X-ray spectroscopy (EDX). The Archimedes drainage method was used to measure the porosity of the sintered samples. X-ray diffractometry (D5000 Siemens) was applied to obtain the XRD spectra with a Cu K_α X-ray source in the 2θ range from 20° and 90° followed by peak matching using MDI Jade V6.0 software. The X-ray diffractometer was used at $0.05^\circ/\text{s}$ with locked scanning rate and mode, respectively. The martensite and austenite transformation temperatures of 12 mg of each sintered sample were identified by differential scanning calorimetry (Q200, TA Instruments) in the scanning range from -80 to $500 \text{ }^\circ\text{C}$ with a heating and cooling rate of $10 \text{ }^\circ\text{C/min}$.

Mechanical Tests

At room temperature of $27 \text{ }^\circ\text{C}$ and constant speed of 0.5 mm/min , an Instron 600 DX-type universal testing machine was used for compression testing. The SME was evaluated using an Instron 600 DX-type universal testing machine with a customized condition and 4% loading strain. Loading and unloading were carried out at $37 \text{ }^\circ\text{C}$, below the martensite start temperature (M_s). Subsequently, the deformed samples were heated to $200 \text{ }^\circ\text{C}$ (above the austenite finish temperature (A_f) for 30 min to recover the residual strain (ε_R); the recovered strain (ε_T) is predominantly attributed to the transformation of detwinned martensite to austenite. The SME and ε_T were calculated using the following formulas:

$$\text{SME} = \frac{L_f - L_o}{L_f}$$

$\varepsilon_T = \frac{\varepsilon_p - \varepsilon_R}{\varepsilon_p} \times 100\%$, where L_f and L_o represent the final and initial length of the compression specimen, respectively, and ε_p is the plastic strain. Vickers microhardness testing was carried out at room temperature of $27 \text{ }^\circ\text{C}$ with an applied load and time of 30 kg and 20 s, respectively.

Electrochemical Tests

Potentiodynamic polarization (PDP) testing was performed using simulated body fluid (SBF) at $27 \text{ }^\circ\text{C}$ to determine the corrosion behavior of the modified and unmodified Ti-51%Ni- x Sn SMAs. The PDP was measured using a surface area of 1 cm^2 in an open-air glass cell containing 300 mL SBF with pH and scan rate of 7.4 and 2 mV/s , respectively. Corrosion data were recorded using a VersaSTAT 3 with a three-electrode cells. The reference, counter, and working electrode were a saturated calomel electrode (SCE), graphite rod, and specimen. The corrosion test was replicated three times to confirm the trend of the obtained results. The corrosion rate (R_i) and polarization resistance (R_p) were calculated according to [23, 24]

$$R_i = 22.85 \times i_{\text{corr}}$$

$$R_p = \frac{\beta_a \beta_c}{2.3(\beta_a + \beta_c)i_{\text{corr}}}$$

where i_{corr} , β_a , and β_c are the corrosion current density and the anodic and cathodic Tafel slope, respectively.

Antibacterial Tests

The antibacterial activity of the Ti-51 at.%Ni- x Sn SMAs was tested on *Escherichia coli* bacteria using the agar disc

diffusion technique (for Gram-negative bacteria) [25]. The bacteria used in this study were obtained from the Kuala Lumpur-based Institute of Medical Research. Before the experiment, the glassware was sterilized in an autoclave at 120 °C for 20 min. The preparation of stock solution of each organism was achieved by mixing 1 ml of each bacterial solution with 9 ml Luria–Bertani (LB) broth followed by incubation for 24 h at 37 °C then shaking at 250 rpm. Solidified nutrient agar swabbing was then carried out using specific organisms ($n = 2$) (1×10^8 CFU/ml) for disc diffusion. In each plate, four discs were fixed at equidistance and subjected to incubation for 24 h at 37 °C. The experiment was carried out thrice, and a digital camera was used to photograph the one with the best image. The average inhibition zone (mm) around the film was measured using ImageJ software (version 1.47).

Results and Discussion

Phase Transformation Temperatures

Figure 1 shows the DSC curves of the Ti-Ni and Ti-Ni-xSn samples, while the transformation temperatures are presented in Table 1. A multistep phase transformation was observed during heating, where $\beta 2$ transformed to R and R transformed to $\beta 19'$ [26–28]. Regarding the transformation

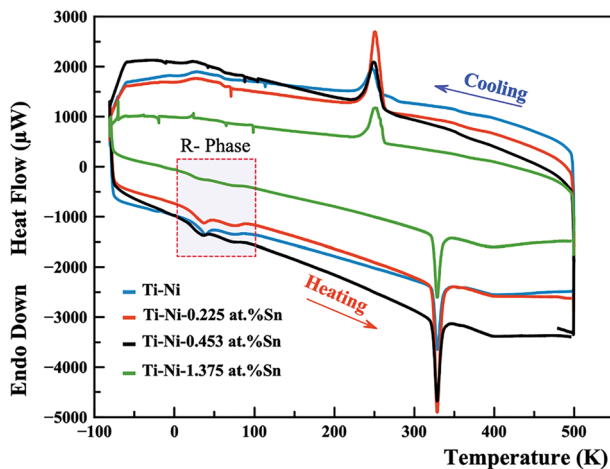


Fig. 1 DSC curves of Ti-Ni-xSn SMA samples

Table 1 Transformation temperatures of Sn-modified and unmodified Ti-Ni SMA alloys

Alloy Ti-Ni-	R_s , K	R_f , K	A_s , K	A_f , K	M_s , K	M_f , K
0 at.% Sn	21	88	318.2	348.4	263	222.7
0.225 at.% Sn	10	93	315.8	350.9	267.3	223.4
0.453 at.% Sn	7	89	316	345.1	268.7	220.4
1.375 at.% Sn	11	44	317.3	344.5	263.9	224.9

temperatures, the martensite start temperature is denoted as M_s , the austenite start temperature as A_s , the martensite finish temperature as M_f , and the austenite finish temperature as A_f . In contrast, the start and finish of the R-phase are denoted as R_s and R_f , respectively.

Practically all NiTiSn SMAs analyzed in literature [17–24] were obtained by using Sn as a replacement at Ni lattice sites instead of Ti lattice sites. Two Hume-Rothery rules support this supposed site preference, i.e., variations in atomic size and electronegativity [29]. Sn has an atomic radius of 1.45 Å, so it is anticipated that it will more easily replace the Ni atom (1.49 Å) than the Ti atom (1.76 Å). Furthermore, the electronic structures of these elements indicate that Sn should favor Ti over Ni lattice sites, although they are very similar (1.91 and 1.96, respectively) relative to Ti (1.54). Furthermore, Sn and Ti prefer to give two electrons, respectively $4d^{10}$ and $4s^2$, to a lower-energy entire shell state, while Ni prefers two electrons. Finally, all three elements have intrinsically distinct crystal structures that provide little insight. Sn's absolute preference for a particular site should be a matter for further investigation because of these differences and the limited studies in the $Ni_{50}Ti_{50-x}Sn_x$ SMA system [23]. According to a number of studies, Sn acts as a stabilizer for α -Ti stabilizers [19–21].

On the other hand, the M_s temperature decreases as the addition of Sn increases to 1.375 wt.% while M_s declines slightly more than R_s , indicating that the R phase transformation separates from the martensite phase transformation. The Ni content is considered an essential factor controlling the behavior of the phase transformation temperatures. In contrast, multistage transformation peaks were found for the low-Ni not high-Ni samples. This can be attributed to a difference in the precipitation kinetics during the addition of the third element (Sn) between the grain boundary and interior. This difference results in preferential precipitation around the grain boundary region but an almost precipitate-free grain interior. Consequently, the martensitic transformation corresponds to B2–R–B19' (two stages) in the grain boundary region but B2–B19' (one stage) in the grain interior.

Gutiérrez-Moreno et al. [29] reported that Ti alloy and low Sn substitutions make the β -phase stable while increasing the Sn concentration induces instability. In other words, addition of large amounts of Sn will have the effect of α -Ti stabilizers, while addition of small amounts of Sn will

have the effect of β -Ti stabilizers. Adding Sn stabilizes the α -phase, resulting in an increase of the α -precipitates/intermetallic compounds [30, 31]. Other peaks can be observed in the DSC curves during cooling. These peaks do not correspond to the martensitic transformation, and their appearance may be related to the effect of stresses formed close to the precipitates upon cooling. This phenomenon was explained in our previous study [32].

Microstructural Characterization

Figure 2a–d shows the microstructure of the Ti-51%Ni SMA samples sintering at 700 °C for 15 min. According to the EDS results, these microstructures show Ti-rich regions as well as Ni-rich regions. Diffusion of Ti towards the Ni element occurred according to the following mechanism: $Ni \rightarrow Ni_3Ti \rightarrow NiTi \rightarrow Ti_2Ni \rightarrow Ti$, and vice versa for Ni

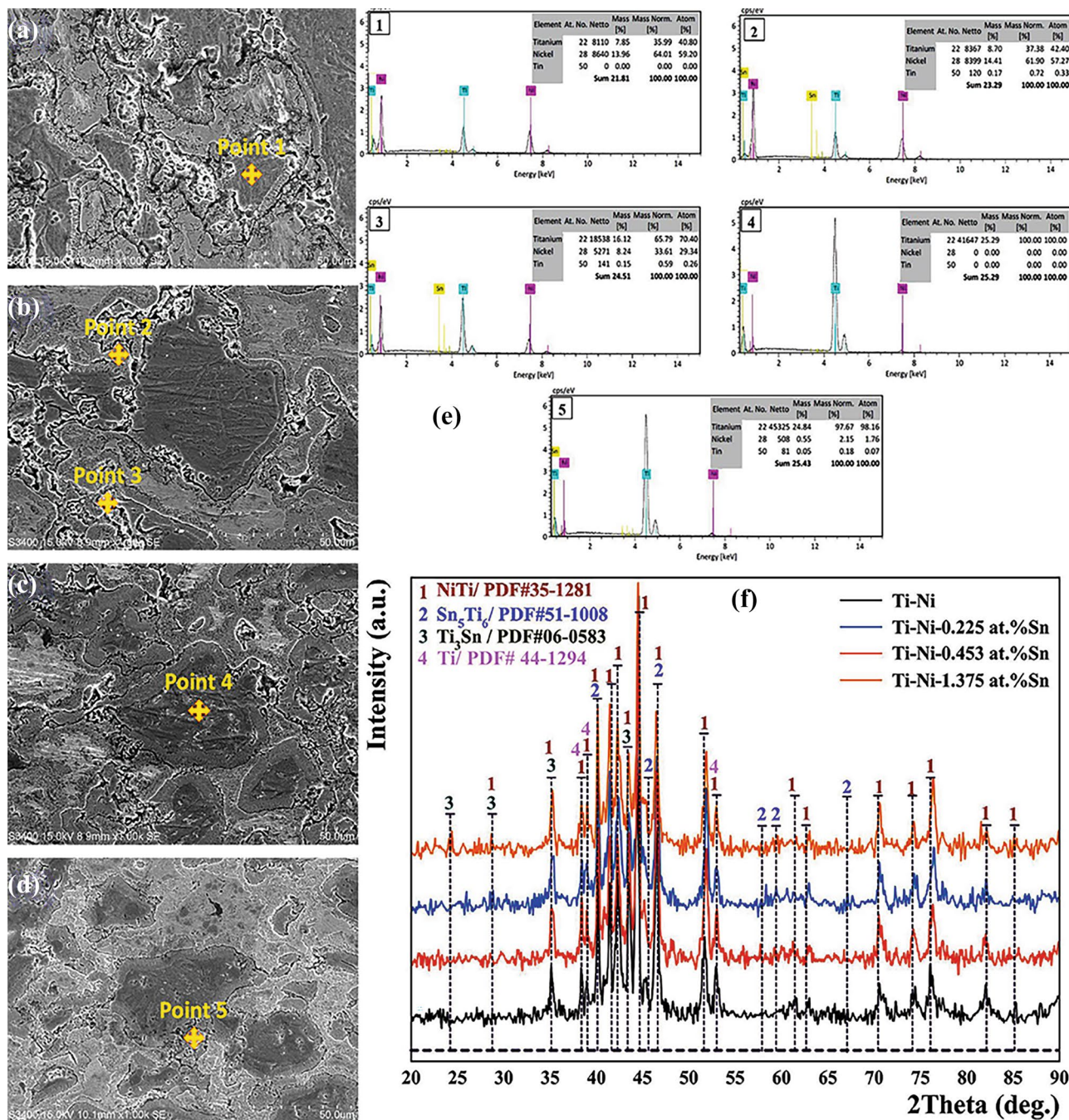


Fig. 2 SEM image and corresponding EDS elemental analysis of Ti-51%Ni-x at.%Sn at the indicated point, where x (at.%) is (a, e1) 0, (b, e2) 0.225, (c, e3) 0.453, and (d, e4) 1.375. **f** X-ray diffraction results of modified and unmodified alloys

diffusion [33]. According to the Ti–Ni phase diagram, the β -Ti and intermetallics compounds [34] are formed alongside plate-like structures that appear clearly after etching with 10% HF-40% HNO₃-50% distilled water solution for 15–30 s. In Fig. 2a, these plates become thinner with addition of Sn. The thickness of these plates gradually reduces with increasing Sn addition (Figure 2b–d), and they disappear at 1.375 at.% Sn.

The density increased after adding Sn, reaching the range of 83.5–87%. The density increased gradually with increasing Sn addition because a low-melting-point addition increases the density of alloys of elements with higher melting points [35]. Figure 2e shows the EDS results for points 1–5 on the micrograph of the Ti–Ni-*x*Sn SMA. Figure 2f shows the Ti–Ni-*x*Sn SMA XRD curves at room temperature, where the Ti–Ni alloys with Sn addition show the typical monoclinic martensite B19' phase. These results indicate that, with Sn addition, the martensite diffraction intensity decreases marginally while the width of the martensite-related peak becomes more significant. The 2θ diffraction angles corresponding to a certain peak are reduced as the Sn content is increased. This indicates that addition of Sn increased the martensite transformation starting temperature (M_s) of the Ti-51 at.%Ni alloy and Sn probably occupied Ni positions in the Ni-rich Ti–Ni alloys. The intensity of the typical peaks reduces marginally while their width increased, so Sn addition distorted the martensitic lattice. The more Sn was added, the greater the distortion. The 2θ reduced, the intensity increased that reflected the volume fraction of martensite.

Mechanical Properties

Compressive Properties of Ti-51%Ni-*x*Sn SMAs

The compressive curves of the Ti–Ni and Ti–Ni-*x*Sn samples are shown in Figure 3. It is possible to divide the compressive curves into three regions [36] with a linear elastic deformation region whereas the elastic modulus that represented by the curve slope of the deformed samples. In the first region with plastic yield deformation the compressive strength of the samples is observed, while the peak stress occurs in the second region. The third region is a rupture region in which rupture has occurred. The fracture strain is enhanced by adding Sn. Indeed, the highest fracture stress and strain is found to the Ti–Ni-0.225Sn sample. Table 2 presents the maximum strength and strain, the calculated Young's modulus, and the hardness of the Ti–Ni-*x*Sn SMA sintered samples. Addition of 0.225Sn to the Ti–Ni sample sintered at 700 °C enhanced the fracture strength and strain, while increasing the Sn content to 0.453 and 1.375 caused a gradual reduction in the fracture strength and its strain. Adding of Sn caused a gradual decrease in the hardness.

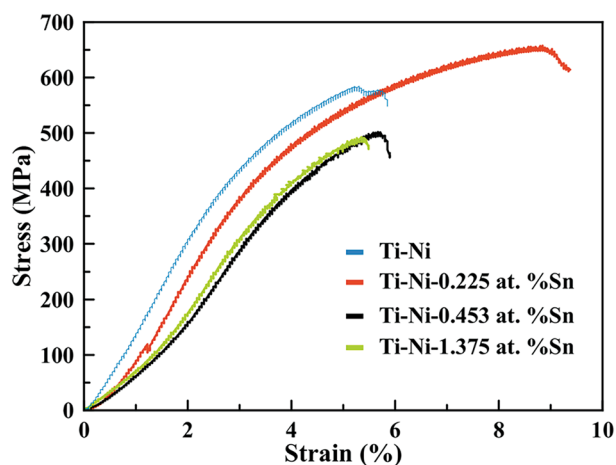


Fig. 3 Compressive curves of Ti-51%Ni-*x*Sn ($x=0.225$, 0.453, and 1.375 at.%) samples microwave sintered at 700 °C

Table 2 Effect of sintering parameters and Sn addition on relative strength, strain, and elastic modulus

Alloy Ti-Ni-	Maximum strength, MPa	Strain at maximum strength, %	Elastic modulus, GPa	Vickers hardness, HV
0 at.% Sn	581	5.26	14.28	152
0.225 at.% Sn	657	8.9	14.2	127
0.453 at.% Sn	499	5.7	12.1	111
1.375 at.% Sn	487	5.4	13	100.7

Also, the low Vickers hardness of these samples before and after adding Sn can be attributed to the microwave sintering method applied and its effect in terms of producing a porous structure and the low elastic modulus [37, 38]. As indicated above, “stress shielding” necessitates the manufacture of alloys with low elastic modulus [10, 39, 40]. Several factors, including precipitate formation, grain size, density, degree of order, and porosity size, shape, structure, and distribution, influence the compression stress and strain. Thus, the density increased with increasing Sn, but the fracture strength and its strain decreased, which can be attributed to the effect of Sn on the α -Ti or β -Ti stabilization.

Shape Memory Effect

The shape memory effect (SME) and total strain recovery (ϵ_T) of the Ti–Ni and Ti–Ni-*x*Sn SMAs with or without Sn addition were determined through a specially designed compression test at $T < M_s$ (human body temperature, 37 °C). Figure 4a shows the shape memory effect results for Ti–Ni and Ti–Ni-*x*Sn. In contrast, Fig. 4b displays the SME, superelastic (SE) recovery, residual strain (ϵ_R), and ϵ_T of the Ti–Ni sample for illustrative purposes. Ti–Ni alloys

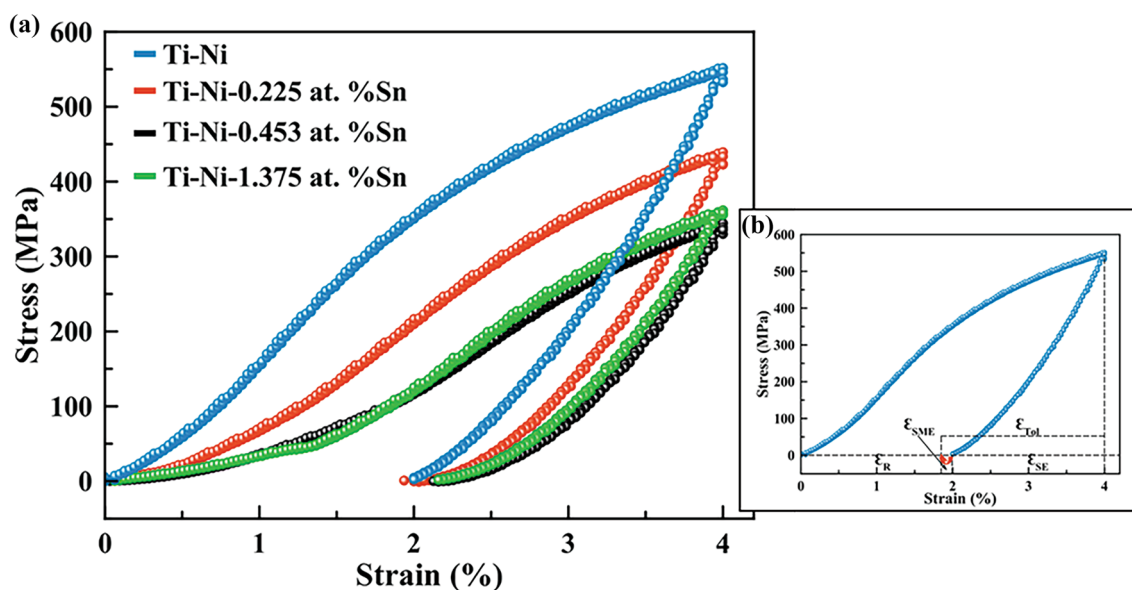


Fig. 4 Shape memory effect test of (a) Ti-Ni and Ti-Ni-xSn and (b) Ti-Ni sample showing SME, SE, ϵ_R , and ϵ_T

Table 3 SME, ϵ_R , and ϵ_T of Ti-Ni-xSn SMAs at 37 °C

Alloy Ti-Ni-	SME, %	Residual strain, ϵ_R , (%)	Total strain recovery, ϵ_T , SE+SME (%)
0 at.% Sn	0.0086	1.9914	50.215
0.225 at.% Sn	0.004	1.9328	51.68
0.453 at.% Sn	0.002	2.1253	46.86
1.375 at.% Sn	0.003	2.156	46.1

sintered at 700 °C exhibited 50.215% total strain recovery or ϵ_T (SE+SME) of the original shape after being heated to a temperature higher than A_f of 200 °C, where SE is the superelastic recovery after releasing the load. The residual strain was 1.9914%. The ϵ_T varied with the amount of Sn addition at the strain value of 4%. It appeared that addition of 0.225 at.% Sn resulted in an increase in the ϵ_T value. The alloy with 0.225 at.% Sn exhibited the highest ϵ_T value after the preheating process at $T > A_f$. Additionally, ϵ_T increased from 50.215 (for the Ti-Ni-based alloy) to 51.68%, while the total strain recovery was 50.215%, 51.68%, 46.86%, and 46.1% for the Ti-Ni-xSn alloys with $x = 0, 0.225, 0.453,$ and 1.375 at.%, respectively. ϵ_R was 1.9914, 1.9328, 2.1253, and 2.156 for the Ti-Ni-xSn samples with $x = 0, 0.225, 0.453,$ and 1.375 wt.%, respectively. However, there were decreases in ϵ_T at 0.453 and 1.375 wt.% Sn compared with 0 and 0.225 wt.% Sn. Table 3 presents the SME, ϵ_R , and ϵ_T of the Ti-Ni-xSn SMAs at 37 °C. The reason for the reduction in ϵ_T with increasing Sn addition above 0.225% may be related to

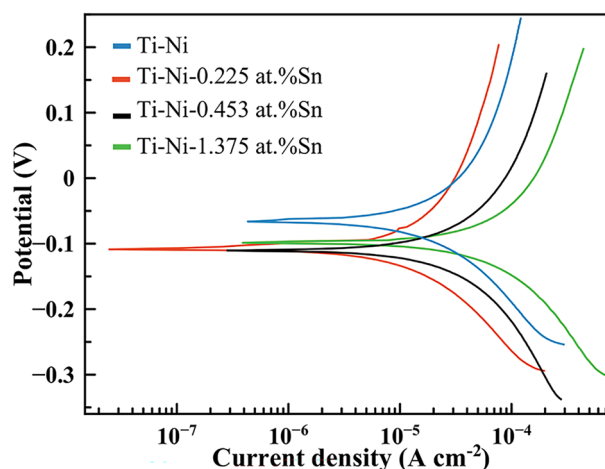


Fig. 5 Potentiodynamic polarization curves in SBF of Ti-Ni and Ti-Ni-xSn sintered at 700 °C for 15 min

the effect of large Sn as a β -Ti stabilizer [29, 41, 42], while the small amounts act as an α -Ti stabilizer [29].

Biocorrosion and Antibacterial Tests

Figure 5 shows the electrochemical polarization curves of the sintered Ti-Ni and Ti-Ni-xSn SMAs in SBF solution. The corrosion potential (E_{corr}) of the Ti-Ni SMA was -65.359 mV. The polarization resistance (R_p) was 1.774 k Ω , and the corrosion rate (R_i) was 0.73508 mm/year. The E_{corr} of the Ti-Ni SMAs was reduced after Sn addition. The

Table 4 Electrochemical parameters of Ti-Ni-Sn samples in SBF solution obtained from polarization testing

Alloys Ti-Ni-	Corrosion potential, E (mV)	Current density, i_{corr} ($\mu\text{A}/\text{cm}^2$)	Cathodic slope, β_c (mV)	Anodic slope, β_a (mV)	Polarization resistance, R_p ($\text{k}\Omega$)	Corrosion rate, R_i (mm/year)
0 at.% Sn	-65.359	32.17	207.099	358.538	1.774	0.73508
0.225 at.% Sn	-106.972	17.84	201.361	445.776	3.38	0.407644
0.453 at.% Sn	-110.111	49.43	1460	2204	7.724	1.129475
1.375 at.% Sn	-98.634	105.3	238.487	391.695	0.612	2.406105

comparison of the current density (i_{corr}) between the binary and ternary SMAs reveals that the Ti-Ni-0.225 at.%Sn SMA demonstrated the most favorable corrosion behavior due to its low R_i in corrosive media. This alloy also presented the lowest i_{corr} value compared with the other alloys with and without Sn addition. The Ti-Ni-0.225Sn SMA had the highest R_p (17.5278 $\text{k}\Omega$) and lowest R_i (0.066447 mm/year). R_i increased gradually with increasing Sn addition to above 0.225 at.%, while R_p rose after adding this proportion of Sn. Table 4 presents the electrochemical parameters of the Ti-Ni and Ti-Ni- x Sn SMAs. Typically, adding Sn to Ti alloys improves their corrosion behavior [22], which may degrade the corrosion behavior after increasing the Sn content to 1% and 3%, which can be attributed to the effect of a large amount of Sn as an α -Ti stabilizer [29]. The potential difference between Ti, Ni, and Sn is minimal in the EMF series. However, addition of Sn to the Ti-Ni alloy increases the corrosion rate (R_i) due to the formation of α and β phases.

Figure 6a and b show the antibacterial activity results for the Ti-Ni and Ti-Ni- x Sn SMA samples against *E. coli*. The results show no clear inhibition zone for the unmodified Ti-Ni SMA, while the average inhibition zone for Ti-Ni- x Sn against *E. coli* was 0.9 mm, 1.2 mm, and 1.5 mm for 0.225, 0.453, and 1.375 at.% Sn, respectively. This can be attributed to binding of metal composites to the outer membrane of *E. coli* bacteria, resulting in more pronounced antibacterial activity with increasing tin addition.

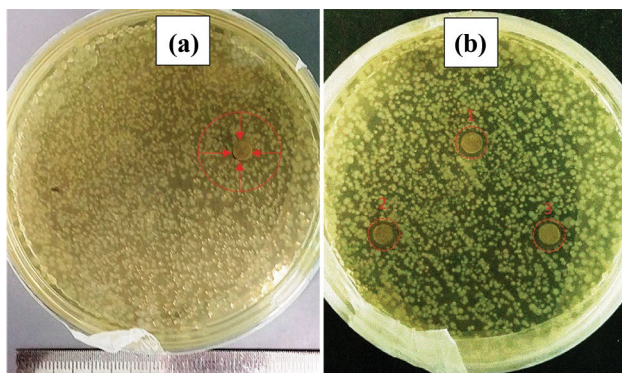


Fig. 6 Inhibition zones against *E. coli* of (a) Ti-Ni, (b-1) Ti-Ni-0.225Sn, (b-2) Ti-Ni-0.453Sn, and (b-3) Ti-Ni-1.375Sn SMA samples sintered at 700 °C

Conclusions

Porous Ti-51 at.%Ni- x Sn ($x = 0, 0.225, 0.453, \text{ and } 1.375$) alloys were successfully fabricated using powder metallurgy and microwave sintering. The mechanical properties showed that the Ti-Ni-0.225%Sn SMA exhibited the highest fracture strength and strain. Due to the microwave sintering process, the lowest Young's modulus and Vickers hardness were mainly attributed to the "stress shielding" effect. The Ti-Ni SMA with 0.225 at.% Sn exhibited the highest ϵ_T after the preheating process at $T > A_f$. On the other hand, the corrosion rate was reduced when adding 0.225% Sn. In contrast, the corrosion resistance was increased, but raising the Sn content above 0.225% increased the corrosion rate and reduced the corrosion resistance. The corrosion potential shifted to lower nobility after adding Sn. Moreover, the average inhibition zone of the Ti-Ni- x Sn samples against *E. coli* gradually increased with increasing Sn addition. In contrast, the Ti-Ni (700 °C) sample did not exhibit an inhibition zone. The favorable effect of Sn addition on the Ti-51Ni SMA makes it more applicable in the biomedical field.

Acknowledgements The authors would like to thank the Ministry of Higher Education of Malaysia and Universiti Teknologi Malaysia for providing financial support under the University Research Grant No. Q.J130000.2524.12H60 and research facilities.

References

1. Y. Liu, The superelastic anisotropy in a NiTi shape memory alloy thin sheet. *Acta Mater.* **95**, 411–427 (2015)
2. R. Artiaga et al., DMTA study of a nickel-titanium wire. *J. Therm. Anal. Calorim.* **70**(1), 199–207 (2002)
3. L.J. Gibson, The mechanical behaviour of cancellous bone. *J. Biomech.* **18**(5), 317–328 (1985)
4. A. Nouri, P. Hodgson, C. Wen, Effect of process control agent on the porous structure and mechanical properties of a biomedical Ti-Sn-Nb alloy produced by powder metallurgy. *Acta Biomater.* **6**(4), 1630–1639 (2010)
5. A. Bansiddhi, T. Sargeant, S. Stupp, D. Dunand, Porous NiTi for bone implants: a review. *Acta Biomater.* **4**(4), 773–782 (2008)
6. I.P. Lipscomb and L.D. Nokes, in *The Application of Shape Memory Alloys in Medicine*, ed. I.P. Lipscomb, L.D.M Nokes (Wiley-VCH, Weinheim, 1996), p. 154

7. H. Hosoda, S. Hanada, K. Inoue, T. Fukui, Y. Mishima, T. Suzuki, Martensite transformation temperatures and mechanical properties of ternary NiTi alloys with offstoichiometric compositions. *Intermetallics*. **6**(4), 291–301 (1998)
8. S. Zlá et al., Determination of thermophysical properties of high temperature alloy IN713LC by thermal analysis. *J. Therm. Anal. Calorim.* **110**(1), 211–219 (2012)
9. A. Kapanen, J. Ryhänen, A. Danilov, J. Tuukkanen, Effect of nickel–titanium shape memory metal alloy on bone formation. *Biomaterials*. **22**(18), 2475–2480 (2001)
10. M. Geetha, A. Singh, R. Asokamani, A. Gogia, Ti based biomaterials, the ultimate choice for orthopaedic implants—a review. *Prog. Mater. Sci.* **54**(3), 397–425 (2009)
11. K. Otsuka, X. Ren, Physical metallurgy of Ti–Ni-based shape memory alloys. *Prog. Mater. Sci.* **50**(5), 511–678 (2005)
12. A. McKelvey, R. Ritchie, Fatigue-crack propagation in Nitinol, a shape-memory and superelastic endovascular stent material. *J. Biomed. Mater. Res.* **47**(3), 301–308 (1999)
13. J. Li, H. Yang, H. Wang, J. Ruan, Low elastic modulus titanium–nickel scaffolds for bone implants. *Mater. Sci. Eng. C*. **34**, 110–114 (2014)
14. D. Wever, A. Veldhuizen, J. De Vries, H. Busscher, D. Uges, J. Van Horn, Electrochemical and surface characterization of a nickel–titanium alloy. *Biomaterials*. **19**(7), 761–769 (1998)
15. S.D. Plant, D.M. Grant, L. Leach, Behaviour of human endothelial cells on surface modified NiTi alloy. *Biomaterials*. **26**(26), 5359–5367 (2005)
16. O. Mockers, D. Deroze, J. Camps, Cytotoxicity of orthodontic bands, brackets and archwires in vitro. *Dent. Mater.* **18**(4), 311–317 (2002)
17. J. Ryhänen et al., In vivo biocompatibility evaluation of nickel–titanium shape memory metal alloy: Muscle and perineural tissue responses and capsule membrane thickness. *J. Biomed. Mater. Res.* **41**(3), 481–488 (1998)
18. T. Duerig, A. Pelton, D. Stöckel, An overview of nitinol medical applications. *Mater. Sci. Eng. A*. **273**, 149–160 (1999)
19. P.J.S. Buenconsejo, H.Y. Kim, S. Miyazaki, Effect of ternary alloying elements on the shape memory behavior of Ti–Ta alloys. *Acta Mater.* **57**(8), 2509–2515 (2009)
20. P.J.S. Buenconsejo, H.Y. Kim, S. Miyazaki, Novel β -TiTaAl alloys with excellent cold workability and a stable high-temperature shape memory effect. *Scr. Mater.* **64**(12), 1114–1117 (2011)
21. H.Y. Kim, T. Fukushima, P.J.S. Buenconsejo, T.-H. Nam, S. Miyazaki, Martensitic transformation and shape memory properties of Ti–Ta–Sn high temperature shape memory alloys. *Mater. Sci. Eng. A*. **528**(24), 7238–7246 (2011)
22. X. Wu, Q. Peng, J. Zhao, J. Lin, Effect of Sn Content on the Corrosion Behavior of Ti-based Biomedical Amorphous Alloys. *Int. J. Electrochem. Sci.* **10**, 2045–2054 (2015)
23. H. Bakhsheshi-Rad et al., Mechanical and bio-corrosion properties of quaternary Mg–Ca–Mn–Zn alloys compared with binary Mg–Ca alloys. *Mater. Des.* **53**, 283–292 (2014)
24. G. Argade, K. Kandasamy, S. Panigrahi, R. Mishra, Corrosion behavior of a friction stir processed rare-earth added magnesium alloy. *Corros. Sci.* **58**, 321–326 (2012)
25. N. Iqbal et al., Characterization and biological evaluation of silver containing fluoroapatite nanoparticles prepared through microwave synthesis. *Ceram. Int.* **41**(5), 6470–6477 (2015)
26. J. Mentz et al., Powder metallurgical processing of NiTi shape memory alloys with elevated transformation temperatures. *Mater. Sci. Eng. A*. **491**(1), 270–278 (2008)
27. B. Yuan, X. Zhang, C. Chung, M. Zhu, The effect of porosity on phase transformation behavior of porous Ti–50.8 at.% Ni shape memory alloys prepared by capsule-free hot isostatic pressing. *Mater. Sci. Eng. A*. **438**, 585–588 (2006)
28. P. Su, S. Wu, The four-step multiple stage transformation in deformed and annealed Ti 49 Ni 51 shape memory alloy. *Acta Mater.* **52**(5), 1117–1122 (2004)
29. J. Gutiérrez-Moreno, Y. Guo, K. Georgarakis, A. Yavari, G. Evangelakis, C.E. Lekka, The role of Sn doping in the β -type Ti–25at% Nb alloys: Experiment and ab initio calculations. *J. Alloys Compd.* **615**, S676–S679 (2014)
30. N. Vellios, P. Tsakiroopoulos, The role of Sn and Ti additions in the microstructure of Nb–18Si base alloys. *Intermetallics*. **15**(12), 1518–1528 (2007)
31. I. Gorna et al., Alloys of the Ti–Si–Sn system (titanium corner): phase equilibria, structure, and mechanical properties. *Powder Metall. Met. Ceram.* **50**(7–8), 452–461 (2011)
32. M.K. Ibrahim, E. Hamzah, S.N. Saud, E. Nazim, N. Iqbal, A. Bahador, Effect of Sn additions on the microstructure, mechanical properties, corrosion and bioactivity behaviour of biomedical Ti–Ta shape memory alloys. *J. Therm. Anal. Calorim.* **131**(2), 1165–1175 (2018)
33. A. Locci, R. Orru, G. Cao, Z.A. Munir, Field-activated pressure-assisted synthesis of NiTi. *Intermetallics*. **11**(6), 555–571 (2003)
34. B.-Y. Li, L.-J. Rong, Y.-Y. Li, V. Gjunter, A recent development in producing porous Ni–Ti shape memory alloys. *Intermetallics*. **8**(8), 881–884 (2000)
35. A. Terayama, N. Fuyama, Y. Yamashita, I. Ishizaki, H. Kyogoku, Fabrication of Ti–Nb alloys by powder metallurgy process and their shape memory characteristics. *J. Alloys Compd.* **577**, S408–S412 (2013)
36. Z. Gao, Q. Li, F. He, Y. Huang, Y. Wan, Mechanical modulation and bioactive surface modification of porous Ti–10Mo alloy for bone implants. *Mater. Des.* **42**, 13–20 (2012)
37. J. Xu et al., Microstructure, mechanical properties and superelasticity of biomedical porous NiTi alloy prepared by microwave sintering. *Mater. Sci. Eng. C*. **46**, 387–393 (2015)
38. J. Xu et al., Effect of pore sizes on the microstructure and properties of the biomedical porous NiTi alloys prepared by microwave sintering. *J. Alloys Compd.* **645**, 137–142 (2015)
39. J. Nagels, M. Stokdijk, P.M. Rozing, Stress shielding and bone resorption in shoulder arthroplasty. *J. Shoulder Elbow Surg.* **12**(1), 35–39 (2003)
40. M. Niinomi, Metallic biomaterials. *J. Artif. Organs*. **11**(3), 105–110 (2008)
41. T. Ozaki, H. Matsumoto, S. Watanabe, S. Hanada, Beta Ti alloys with low Young’s modulus. *Mater. Trans.* **45**(8), 2776–2779 (2004)
42. Q.-M. Hu, S.-J. Li, Y.-L. Hao, R. Yang, B. Johansson, L. Vitos, Phase stability and elastic modulus of Ti alloys containing Nb, Zr, and/or Sn from first-principles calculations. *Appl. Phys. Lett.* **93**(12), 121902 (2008)

Publisher’s Note Springer Nature remains neutral with regard to jurisdictional claims in published maps and institutional affiliations.